Supplementary Information for "A long-term record of Antarctic ice sheet loss during millennial-scale ocean warming" by G. Piccione, T. Blackburn, S. Tulaczyk, E.T. Rasbury, M. Hain, D.E. Ibarra, K. Methner, C. Tinglof , B. Cheney, P. Northrup[2], K. Licht

^{234}U-^{230}Th dating

^{234}U-^{230}Th dates were produced at the University of California Santa Cruz (UCSC) Keck Isotope Laboratory. Samples were spiked with a gravimetrically calibrated mixed ^{229}Th-^{236}U tracer for isotope dilution analyses. They were then digested in 3mL 7N HNO_3 (calcite) or concentrated 4mL HF + HNO3 (opal) via benchtop dissolution and dried down. U and Th separates were purified using ion chromatography with 1mL columns of 200-400 mesh, AG1-X8 anion resin. Samples were loaded onto the column in 1mL of 7N HNO_3 and major elements were washed off with an additional 2ml HNO_3. Loading and washing eluant was collected and saved for Sr analyses. Thorium was eluted in 2mL of 6N HCl. Uranium was then eluted in 2mL of ultra-pure water. This column procedure was then repeated to achieve U and Th purity levels necessary for analyses. Total procedural blanks were <10pg for U and <25pg for Th, which are minor relative to sample concentrations. Both U and Th isotopic measurements were conducted using the IsotopX X62 Thermal Ionization Mass Spectrometer (TIMS) housed at UCSC. U and Th samples are loaded onto 99.99% purity Re ribbon. Uranium is loaded in a Si-gel activator and measured as UO_2. Uranium compositions were corrected for oxide isobaric interferences following ref.[1]. Uranium measurements were performed as a two sequence "Fara-Daly" routine: in the first sequence, ^{234}U (mass 266) is collected on the Daly, while ^{235}U (mass 267) and ^{238}U (mass 270) is collected on the high Faraday cups equipped with $1e^{12}$ Ω resistors. The second sequence placed ^{235}U (mass 267) on the Daly and ^{236}U (mass 268) and ^{238}U (mass 270) on the high Faraday cups. The 266(Daly)/270(Faraday) composition was corrected using the Fara-Daly gain: (267Faraday/270Faraday) / (267Daly/270Faraday). Uranium compositions were corrected for oxide isobaric interferences following ref.[1]. Mass dependent fractionation correction was applied using a linear correction with correction factor determined from long-term measurement of standards. Uranium dead times for the Daly were calibrated using NBS U-500. Accuracy of the uranium method is evaluated using Uranium standard NBS4321 (Extended Data Fig. 7). Thorium isotope measurements were also done on the TIMS at UCSC. Thorium is loaded in a graphite emitter and measured as a metal. Each mass of Th is measured using a peak hopping routine on the Daly. Thorium fractionation and deadtime were estimated by running NBS U 500 as a metal. Accuracy of ^{234}U-^{230}Th dates were tested using MIS 5e coral and compared to dates in ref [2], as well as a previously dated carbonate precipitate[3]. U-Th ages are calculated using codes designed at UCSC. No reported ages assume an initial [^{230}Th/ ^{232}Th], as uranogenic contribution is sufficiently large ([^{230}Th/ ^{232}Th]>20) that ages are insensitive to the composition of initial thorium. Decay constants for all data and models were from ref. [4]. All uncertainties are reported at 2σ, unless otherwise specified.

Reduced complexity ice sheet model

We use a reduced complexity model of ice thermodynamics to demonstrate that there is a glaciologically plausible mechanism for explaining the two key observations derived from the precipitate samples MA113 and PRR50489: (i) cyclic opal-calcite precipitation from subglacial waters switching between oxygen- and carbon-poor brines and carbon- and oxygen-rich meltwaters, and (ii) the timing of opal layers with cold phases of AIMs cycles and calcite layers with the warm phases of these cycles. Combined, these observations indicate that the subglacial water bodies in which these two precipitates formed, although separated by ca. 1000 km distance, experienced hydrologic isolation and cryoconcentration during cold AIM phases and became open to basal meltwater inputs during warm phases. Glaciologically, the most parsimonious explanation is that the cold AIM phases corresponded to basal freezing conditions while warm phases to basal melting conditions in the two areas of sample formation.

Switches between basal melting and freezing conditions are controlled by the basal thermal energy balance, E. The three most fundamental controls on E are two sources of heat (G = geothermal heat flow and S = shear heating accompanying ice motion), and one sink of heat (Q = conductive heat loss) (e.g., Tulaczyk et al., 2000):

$$E=G+S-Q \quad \text{Eq. S1}$$

There is no physical reason for geothermal heat flow to vary on the timescale of AIMs. Hence, we treat it as a time invariable parameter with a value of 0.05 W/m^2 [1]. Changes in surface temperature and accumulation rate accompanying AIMs can impact the basal thermal energy balance through the conductive heat loss term, Q, but the ice sheet does mute this effect through[2]: (i) dampening the amplitude of temperature variations with depth, and (ii) introducing a time lag between surface climate forcing and basal thermal response. In ref. [2] authors pointed out that a under the purely conductive vertical heat transport, a periodic surface temperature forcing will decay exponentially with e-folding depth scale of 314 m. Given that the potential sample source areas have ice thicknesses of about 1500m[3–5], an AIM-scale surface temperature fluctuations of 1-3°C[6,7] would amount to 0.008-0.025°C change in ice temperature near the bed. Using equation 1 from ref. [8] we calculated that, even assuming an instantaneous thermal equilibration throughout ice thickness, the maximum difference between the conductive heat loss during cold and warm AIM phases would be about 0.001 W/m^2 (assuming ice thickness of 1500m, temperature change of 3°C, and accumulation rate of 0.03 m/yr during the warm phase and 0.02 m/yr during the cold phase[9]. This is more than an order of magnitude less than the assumed geothermal flux. We will show later that it is also one to two orders of magnitude less than the contribution from the shear heating term, S.

The second fundamental problem with relying on vertical advection and diffusion of surface climate signals to the bed is the significant time lag with which such a transfer happens (e.g., ref. [2]). The timescale for purely conductive heat transfer can be estimated from the ratio of the square of ice thickness (H) to the thermal diffusivity of ice, which for H of 1500 m and diffusivity of 44 m^2/yr [2] yields ca. 50,000 years. The equivalent timescale for the purely advective vertical heat transfer can be approximated as the ratio of the ice thickness to the surface accumulation, which for reasonable assumptions of 1500m and 0.03 m/yr [9], respectively, also yields 50,000 years. The low accumulation rates assumed for the regions of interest are justified by both, ice sheet modeling of ice sheet sensitivity to AIM forcing[4], and the fact that the two samples were found in locations where under modern conditions the surface mass balance is negative[10,11]. Given that these diffusive and advective time scales are about an order of magnitude longer than the millennial-scale AIM climate fluctuations, we do not favor variations in the conductive heat loss term (Q in equation S1) as an explanation for the cyclicity in subglacial hydrological conditions inferred from our samples.

By the process of elimination, we arrive at the shear heating term, S, in equation S1 as the most promising mechanism for triggering switches between basal melting and freezing conditions on millennial timescales. Given the slow ice motion at, and upstream of, sample collection locations[5], we approximate the shear heating term, S, as a product of the driving shear stress and deformational ice velocity, U, averaged over ice thickness:

$$S = \tau U = \frac{2A}{n+2}\tau^{n+1}H = \frac{2A}{n+2}(\rho g \alpha)^{n+1}H^{n+2} \quad \text{Eq. S2}$$

where τ =gravitational driving stress ($\rho g H \alpha$), ρ = ice density, g = gravitational acceleration, H = ice thickness, α = ice surface slope, n = stress exponent in the ice flow law (assumed to be 3, ref. [12], table 3.3), A = ice viscosity parameter (the value for ice at 0°C in the table 3.4 in ref. [12]). We follow the simplifying assumption that all shear heating can be attributed to ice motion at/near the basal interface[13].

Equation S2 contains two glaciological variables that vary with climate forcing, the ice surface slope and ice thickness. Since the latter is raised to a higher power (H^5) than the former (α^4), perhaps ice thickness is the preferred pathway through which millennial scale climate changes have influenced shear

heating in the two sample formation areas? To match the observed precipitation patterns, ice thickness would have to increase during warm AIM phases and decrease during AIM cold phases. Output from the model simulations in ref. [4], which examined the response of the Antarctic ice sheet to AIM climate forcing, shows the ice thickness decreasing with increasing temperature in both regions from which our samples have been collected. This means that any tendency for ice to thicken as accumulation rate increases is readily overcome by an increase in the dynamic ice thinning associated with the grounding line retreat and ice flow acceleration during warm AIM phases[4]. This dynamic effect enters our simplified model of shear heating (Equation S2) through the ice surface slope, which steepens when the ice in the Ross Embayment thins because of grounding line retreats (AIM warm phases) and becomes shallower when ice sheet thickness in the Ross Embayment increases during grounding line advance (AIM cold phases).

In our calculations of time-dependent shear heating we parametrize the evolution of regional ice surface slope along an ice drainage pathway connecting a sample origination region to the Ross Embayment:

$$\alpha(t) = [\Delta b + H(t) - H_{RE}(t)]/L_o \qquad \text{Eq. S3}$$

where $\Delta b =$ bedrock elevation difference between the region from which a sample originated and the part of the Ross Embayment into which ice from this region is draining (at the foothills of Transantarctic Mountains), $H(t) =$ ice thickness in the region of sample origin, $H_{RE}(t) =$ ice thickness at the foothills of Transantarctic Mountains, $L_o =$ a length scale representing the distance between the sample origination region and the ice discharge area in the Ross Embayment (assumed to be ~100 km). The bedrock elevation difference is estimated from existing bed elevation datasets[3,5]. Ice thickness forcing at the foothills of Transantarctic Mountains, $H_{RE}(t)$, is parametrized as a linear function of an ice core isotopic record of paleoclimate, $i(t)$, covering the time periods of sample precipitation:

$$H_{RE}(t) = H_o + C_i[i(t) - i_o] \qquad \text{Eq. S4}$$

where $H_o =$ is the initial thickness (taken from ice sheet model output of ref. [4]), $C_i =$ proportionality constant with units of meters per ‰, and $i_o =$ the initial isotopic value in ‰. For simulations of basal thermal conditions pertaining to the sample MA113 we use the $d^{18}O$ record from the WAIS Divide ice core[14] and for the older sample PRR50489 we use the dD record from the EDC ice core[15]. In our model the ice thickness in the sample formation area, $H(t)$, evolves through time following this simple mass-balance ODE:

$$\frac{\partial H(t)}{\partial t} = aL_a - UH(t) \qquad \text{Eq. S5}$$

where $t =$ time, $a =$ accumulation rate (0.02-0.03 m/year taken from the ice sheet model output of ref. [4]), and $L_a =$ accumulation length scale (i.e., taken to be 500 km as the approximate length of the accumulation zone upstream of the site where $H(t)$ is evaluated.

To produce the output shown in Figure 1 of the main manuscript text, we solved numerically the system of equations S1 through S5 using a forward-difference solver with time step of 10 years and a set of the necessary initial conditions. Each simulation was started 10,000 years before the beginning of the two precipitate records to provide model time for relaxation of the calculation from any artifacts associated with our choice of initial conditions. The basal thermal energy budget is expressed by us in terms of equivalent basal melting/freezing rate in units of mm/year using the volumetric latent heat of ice 3×10^8 Joules/m^3. The key tunable model parameter is C_i, the constant determining the sensitivity of ice thickness changes to variations in isotopic records of paleoclimate (Equation S4). The sensitivity of our results to C_i is illustrated in Figure S1(a). For the set of control parameters used to generate Figure S1a, the basal heat budget experiences switches between melting and freezing in the right time periods to explain changes between opal and calcite if the C_i parameter is between 10 and 23. A too low value does not yield the

expected melting-freezing switches in the last 15,000 years of the record (e.g., $C_i = 5$ in Figure S1a). A too high value results in output that predicts too long freezing period between 180 and 200 kyrs BP (e.g., $C_i = 25$ in Figure S1a). The satisfactory results $C_i = 10$ to 23, are consistent with ice thickness changes in the Ross Embayment, $H_{RE}(t)$, of a few to several hundreds of meters on the millennial scale of AIM climate cycles. This magnitude of ice thickness variations corresponds to the cases of high sensitivity of the Antarctic ice sheet to ocean thermal forcing in numerical experiments of ref. [4]. Figure S2 shows equivalent results for the sample MA113, with $C_i = 10$, 50, and 250 in units of m/‰ of $\delta^{18}O$ (since we are using the WAIS Divide ice core record for this sample). Generally, satisfactory results are obtained for MA113 when C_i is between ca. 50 and 200. Too low values produce not enough switches too basal freezing in the second half of the record while too high values are missing some switches to basal melting (e.g., Figure S2). Ice thickness changes that produce satisfactory results are in the range of a few hundred meters variation in $H_{RE}(t)$. This range is somewhat lower than that for the other sample. However, given this more interior sample location, this result is still consistent with the ice sheet model runs of ref. [4] that assume high sensitivity to the ocean thermal forcing.

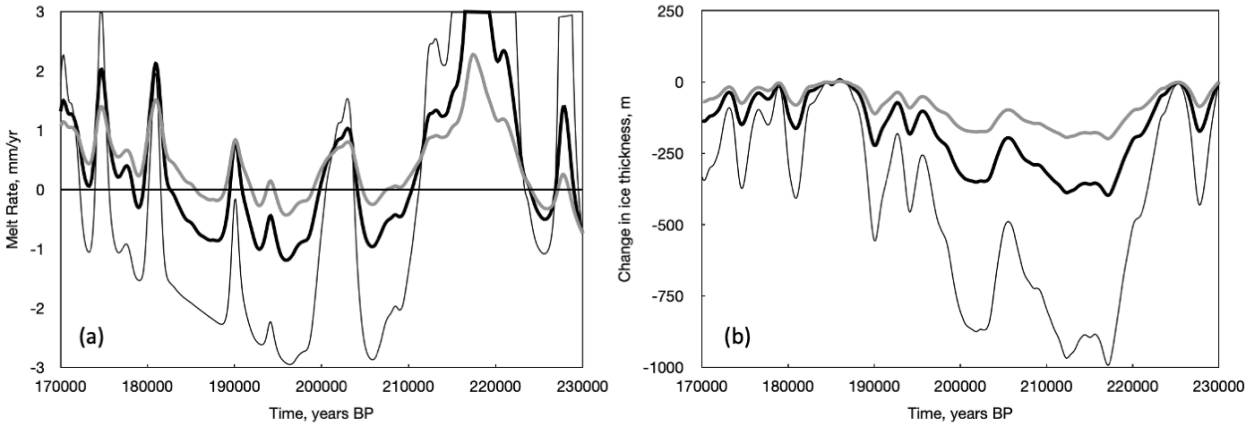

Figure S1 | Reduced Complexity Ice Sheet Model Outputs for Sample PRR50489. a. Sensitivity of the basal thermal energy balance, expressed in terms of equivalent basal melt (+) or freeze (-) rate given in mm/year. The thick black line shows the preferred scenario for C_i = 10 m per ‰ of dD from the EDC ice core record. The thin black line gives the C_i = 25 scenario and the thick grey line is for the C_i = 5 case. **b.** Equivalent changes in ice thickness, $H_{RE}(t)$, which represent the impact of climate forcing on our model through equation S4. The same types of lines as in **a.** are used here to represent the three cases $C_i = 5$, 10 and 25.

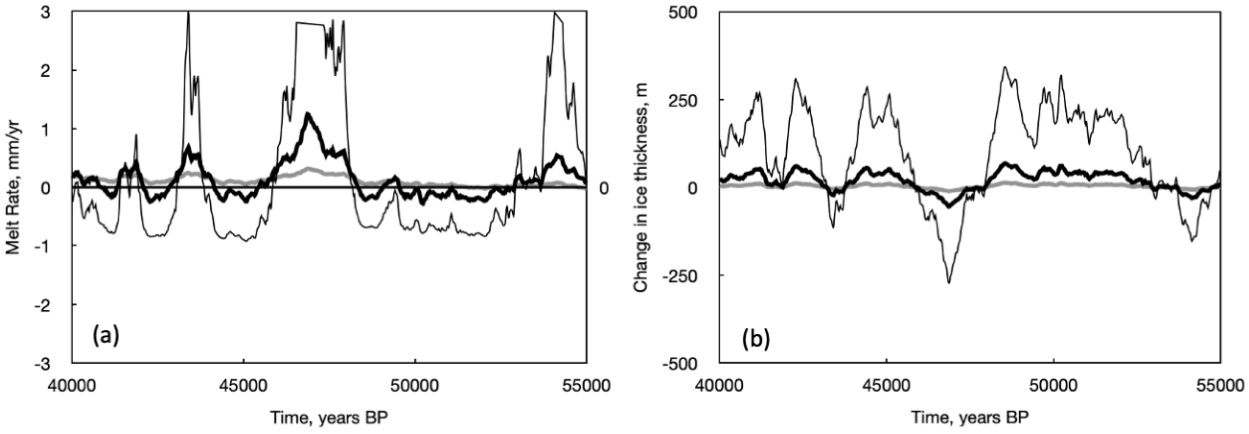

Figure S2 | Reduced Complexity Ice Sheet Model Outputs for Sample MA113. Plots equivalent to those in Figure S1 but for simulations pertaining to the sample MA113 and with C_i = 10, 50, and 250 of m per ‰ of, corresponding to the thick grey lines, **a.** Sensitivity of the basal thermal energy balance, expressed in terms of equivalent basal melt (+) or freeze (-) rate given in mm/year. The thick black lines show the preferred scenario for C_i = 50 m per ‰ of $d^{18}O$ from the WAIS Divide ice core record. The thin black lines give the C_i = 250 scenario and the thick grey lines are for the C_i = 10 case.

Additional References

1. Goodge, J. W. Crustal heat production and estimate of terrestrial heat flow in central East Antarctica, with implications for thermal input to the East Antarctic ice sheet. *Cryosphere* **12**, 491–504 (2018).

2. MacAyeal, D. R. Binge/purge oscillations of the Laurentide Ice Sheet as a cause of the North Atlantic's Heinrich events. *Paleoceanography* **8**, 775–784 (1993).

3. Fretwell, P. *et al.* Bedmap2: Improved ice bed, surface and thickness datasets for Antarctica. *Cryosphere* **7**, 375–393 (2013).

4. Blasco, J., Tabone, I., Alvarez-Solas, J., Robinson, A. & Montoya, M. The Antarctic Ice Sheet response to glacial millennial-scale variability. *Clim. Past* **15**, 121–133 (2019).

5. Matsuoka, K. *et al.* Quantarctica, an integrated mapping environment for Antarctica, the Southern Ocean, and sub-Antarctic islands. *Environ. Model. Softw.* **140**, (2021).

6. Barbante, C. *et al.* One-to-one coupling of glacial climate variability in Greenland and Antarctica. *Nature* **444**, 195–198 (2006).

7. Buizert, C. *et al.* The WAIS Divide deep ice core WD2014 chronology – Part 1: Methane synchronization (68-31 ka BP) and the gas age-ice age difference. *Clim. Past* **11**, 153–173 (2015).

8. Begeman, C. B., Tulaczyk, S. M. & Fisher, A. T. Spatially Variable Geothermal Heat Flux in West Antarctica: Evidence and Implications. *Geophys. Res. Lett.* **44**, 9823–9832 (2017).

9. Cauquoin, A. *et al.* Comparing past accumulation rate reconstructions in East Antarctic ice cores using 10Be, water isotopes and CMIP5-PMIP3 models. *Clim. Past* **11**, 355–367 (2015).

10. Bintanja, R. On the Glaciological, Meteorological, and Climatological Significance of Antarctic Blue Ice Areas. *Rev. Geophys.* **37**, 337–359 (1999).

11. Kassab, C. M. *et al.* Formation and evolution of an extensive blue ice moraine in central Transantarctic Mountains, Antarctica. *J. Glaciol.* **66**, 49–60 (2019).

12. Cuffey, K. M. & Paterson, W. S. . B. *Physics of Glaciers, Fourth Edition*. *The Physics of Glaciers* (2010).

13. Ritz, C. Time dependent boundary conditions for calculation of temperature fields in ice sheets. *Int. Assoc. Hydrol. Sci.* **170**, 207–216 (1987).

14. Members, W. D. P. Precise interpolar phasing of abrupt climate change during the last ice age. *Nature* **520**, 661–665 (2015).

15. Jouzel, J. *et al.* Orbital and millennial antarctic climate variability over the past 800,000 years. *Science (80-.).* **317**, 793–796 (2007).